Energetic near-inertial waves induced by winter storms and mesoscale eddies in the subtropical Northwestern Pacific Ocean

Hongkai Wang[1,3], Zifei Chen[1], Xinyuan Diao[1,2,3], Fei Yu [1,2,3], Xingchuan Liu[1], Qiang Ren[1], Feng Nan[1,2,3]

[1] Key Laboratory of Ocean Observation and Forecasting & Laboratory of Ocean Circulation and Waves, Institute of Oceanology, Chinese Academy of Sciences, Qingdao, 266071, China
[2] Laboratory for Ocean Dynamics and Climate, Qingdao Marine Science and Technology Center, Qingdao, 266071, China
[3] College of Marine Sciences, University of Chinese Academy of Sciences, Beijing 100049, China

Correspondence to: Zifei Chen (chenzifei@qdio.ac.cn), Fei Yu (yuf@qdio.ac.cn)

Abstract. Near-inertial waves (NIWs) play a fundamental role in transferring wind energy into the ocean interior and sustaining diapycnal mixing, yet their wintertime characteristics and interactions with mesoscale eddies remain insufficiently understood. Using subsurface mooring observations and reanalysis products in the subtropical Northwestern Pacific Ocean, we investigate the generation, downward propagation, and modal characteristics of NIWs associated with two winter storm events. Although the wind energy input into the mixed layer during the first storm is approximately three times larger than that during the second storm, the observed near-inertial kinetic energy (NIKE) in the thermocline is comparable between the two events. Energy transfer analyses show that mesoscale eddies extract about 46% of the wind-generated near-inertial energy during the first event, whereas they supply approximately 43% of the wind input to NIWs during the second event. Although the opposing transfers may contribute to the comparable NIKE observed during the two events, given the observational limitations, the terms of near-inertial energy radiation out of the observed region and energy dissipation cannot be quantified directly but may also contribute to the observed NIKE. Additionally, the two NIW events exhibit distinct vertical wavelengths, group velocities, and modal structures. The first event is characterized by a larger vertical wavelength, faster downward group velocity, and dominance of low baroclinic modes, with the first four modes accounting for nearly half of the total NIKE. In contrast, the second event displays shorter vertical wavelengths and enhanced high-mode energy, with modes five to eight contributing about 41% of the total NIKE. These differences are attributed to the combined effects of mesoscale eddy modulation and the modal projection of wind energy. Our results highlight the critical roles of winter storms and eddy-wave interactions in shaping the energy, propagation, and modal characteristics of NIWs.

1 Introduction

Near-inertial waves (NIWs) are widely observed throughout the global ocean and exhibit prominent spectral energy near the local inertial frequency f_0 ($f_0 = 2\Omega\sin\varphi$, where Ω is the angular velocity of the Earth and φ is the local latitude), possessing nearly half of the kinetic energy in the internal wave field (Kunze, 1985; Garrett, 2001; Ferrari and Wunsch, 2009; Alford et al., 2016). NIWs are primarily generated by time-varying winds such as hurricanes, typhoons, and winter storms (D'Asaro, 1985; Shay and Jaimes, 2010; Chen et al., 2023). In their horizontal and vertical propagation processes, NIWs nonlinearly deform into shorter vertical wavelengths and eventually break, resulting in enhanced turbulent mixing in the ocean interior (Alford, 2003a; Whalen et al., 2020). Therefore, NIWs play a crucial role in transferring energy from the atmosphere to the ocean and contributing to diapycnal mixing (MacKinnon and Gregg, 2003; Alford et al., 2012).

Munk and Wunsch (1998) estimated that ~2.1 TW (1 TW = 10^{12} W) of power is needed to sustain the global meridional overturning circulation and abyssal stratification. Internal tides generated by interactions between tides and topography supply ~0.9 TW (Egbert and Ray, 2001; de Lavergne et al., 2019; Vic et al., 2019; Buijsman et al., 2020), while the remaining ~1.2 TW is mainly from wind forcing (Wunsch, 1998). Energetic wind-induced near-inertial energy in the mixed layer can radiate into the interior of the ocean, providing energy for deep ocean mixing (Alford et al., 2016). Using a mixed layer slab model developed by Pollard and Millard (1970), the global near-inertial wind power in the mixed layer is estimated to be between 0.3 and 1.5 TW (Watanabe and Hibiya, 2002; Alford, 2003b; Jiang et al., 2005; Rimac et al., 2013; Liu et al., 2019). However, Furuichi et al. (2008) suggested that the near-inertial wind power penetrating from the mixed layer into the interior of the ocean amounts to only approximately 0.1 TW, far below the energy required to maintain interior diapycnal mixing.

In addition to wind forces, the net energy input from mesoscale eddies to NIWs can serve as a crucial additional energy source for sustaining interior diapycnal mixing (Ferrari and Wunsch, 2009; Polzin, 2010; Alford et al., 2016; Thomas and Daniel, 2020). The strain structure of the background flow is a key factor in controlling energy conversion between mesoscale eddies and internal waves (Polzin, 2010). Using a long-term mooring array data obtained in the northern Gulf of Mexico, Jing et al. (2018) indicated that Okubo-Weiss (OW) parameter governs the magnitude of energy transfer rate, with positive OW parameters indicating a pronounced energy exchange between mesoscale eddies and NIWs. Through numerical simulations, Barkan et al. (2021) suggested that ~25% of mesoscale eddy energy is forward transferred to the internal wave field. Using subsurface mooring observations combined with reanalysis data, Chen et al. (2023) pointed out that net energy transfer from an anticyclonic eddy to the NIWs significantly amplifies the near-inertial kinetic energy, accounting for about 71 % of the wind energy input. Using global drifter observations, Liu et al. (2023) indicated that the mean integrated energy transfer rate is 0.025 TW from eddies to NIWs, with a particularly notable energy transfer efficiency observed in anticyclonic eddies. Through a realistic numerical simulation in the California Current, Delpech et al. (2023) suggested that interactions between eddies and NIWs are more efficient, thereby providing a significant portion of energy required to sustain oceanic diapycnal mixing.

To understand the spatial distribution of diapycnal mixing shaped by the breaking of internal waves, modal decomposition has been widely used to analyze modal content and propagation characteristics of NIWs (e.g., Alford, 2020; Musgrave et al., 2022; Cao et al., 2023; Kawaguchi et al., 2023; Zheng et al., 2023a). Generally, modal content of internal waves is mainly related to the mixed layer depth (MLD). As MLD increases, the energy proportion of low modes tends to increase (Alford et al., 2016; Guthrie and Morison, 2021). When near-inertial energy is primarily projected into low modes, NIWs can typically propagate horizontally and vertically to locations far from their generation region (Alford, 2003a; 2010). In contrast, when near-inertial energy is dominated by high modes, the waves are more prone to breaking, thereby promoting local diapycnal mixing (Simmons and Alford, 2012). Cao et al. (2021) suggested that NIWs generated by the Typhoon Megi can propagate to a depth of approximately 1000 m due to the dominance of the first three modes in near-inertial energy. Based on a global realistic simulation, Raja et al. (2022) revealed that over half of the sum of the wind-generated near-inertial energy is projected on the first five modes.

The subtropical Northwestern Pacific Ocean is a hotspot characterized by energetic wind energy input and abundant mesoscale eddies. The mooring site at 25°N, 146°E is located near the northern flank of the North Pacific Subtropical Countercurrent (STCC) band. In this region, the shallow eastward-flowing STCC overlies the subsurface westward North Equatorial Current, forming a vertically sheared current system that is favorable for baroclinic instability and contributes to energetic mesoscale eddy field (Qiu, 1999; Qiu and Chen, 2010). Although tropical cyclones are drastic synoptic events, winter storms remain an important source of near-inertial energy in this region (e.g., Zheng et al., 2022). Compared with tropical cyclones, winter storms are characterized by larger spatial scales and longer durations (Bieli et al., 2020; Cheung et al., 2025). In addition, active mesoscale eddies in this region can lead to prominent interactions between mesoscale eddies and NIWs (Qiu, 1999). Due to strong wind stirring and weak stratification in winter, the mixed layer depth is evidently deeper than that in summer (de Boyer Montégut et al., 2004). However, the propagation and characteristics of storm-induced NIWs in the subtropical Northwestern Pacific Ocean remain insufficiently understood.

Combined with subsurface mooring observations and reanalysis products in the subtropical Northwestern Pacific Ocean, we found that during two winter storms, the wind-generated near-inertial energy input differed markedly, whereas the observed near-inertial kinetic energy was comparable. Motivated by this contrast, the generation and characteristics of these two NIW events were investigated in this study. Specifically, mesoscale eddies extract about 46% of the wind-generated near-inertial energy during the first NIW event, whereas they supply an amount equivalent to about 43% of the wind input to NIWs during the second NIW event. In addition, we examine how mesoscale eddy modulation, together with the modal projection of wind energy, contributes to differences in the modal content of the two NIW events. The remainder of this paper is organized as follows. Data and methods are presented in Section 2. Section 3 describes the characteristics of NIWs during the two winter storms. Section 4 discusses the energy exchange between NIWs and mesoscale eddies, as well as the possible mechanisms responsible for the difference in modal composition of the two near-inertial events. Finally, a summary is presented in Section 5.

2 Data and methods

2.1 Data

From April 2017 to June 2018, a subsurface mooring was deployed at 146°E, 25°N in the subtropical Northwestern Pacific Ocean, where the local water depth is approximately 5692 m (Fig. 1a). The instruments equipped in the mooring include two

Teledyne RDI Workhorse Long Ranger 75-kHz acoustic Doppler Current Profilers (ADCPs), eight SBE 37-SM instruments (CTD37), and eleven SBE 56 temperature loggers in the upper 1000 m (Fig. 1b). The upward-looking and downward-looking Teledyne RDI Workhorse Long Ranger 75-kHz ADCPs were mounted at 400 m depth, and jointly provided valid velocity measurements in the upper 900 m depth. The ADCPs sampled at an interval of 1 h with a vertical bin size of 8 m. The raw ADCP data were subjected to quality control procedures including removal of bins affected by sidelobe contamination, screening based on correlation, percent good, velocity error, and removal of velocity spikes. The SBE 37-SM conductivity, temperature, and pressure records and the SBE 56 temperature records were processed using the manufacturer calibration coefficients and subsequently checked for spikes and physically unrealistic values. According to the prominent near-inertial motions observed by the subsurface mooring during the winter period, the data collected from 20 November, 2017 to 31 January, 2018 are used in this study. The depth-time plot of the raw velocities is shown in Figs. 1(c-d).

Wind field data were obtained from the fifth major global reanalysis produced by the European Center for Medium-Range Weather Forecasts (ERA5). Thus, the wind stress vector, $\boldsymbol{\tau}$, and near-inertial velocity vector, $\boldsymbol{v}_{\mathrm{ni}}$, can be calculated via the parameterization of Oey et al. (2006) and the slab model of Pollard and Millard (1970) (with a damping parameter of 0.06 f_0), respectively. A comparison between the slab model derived near-inertial velocity and the observational near-inertial velocity is provided in Fig. S2 of the supplementary material. Sea level anomaly (SLA) and surface geostrophic velocity data were obtained from satellite altimetry products provided by Ssalto/Duacs and distributed through the Copernicus Marine Environment Monitoring Service (CMEMS).

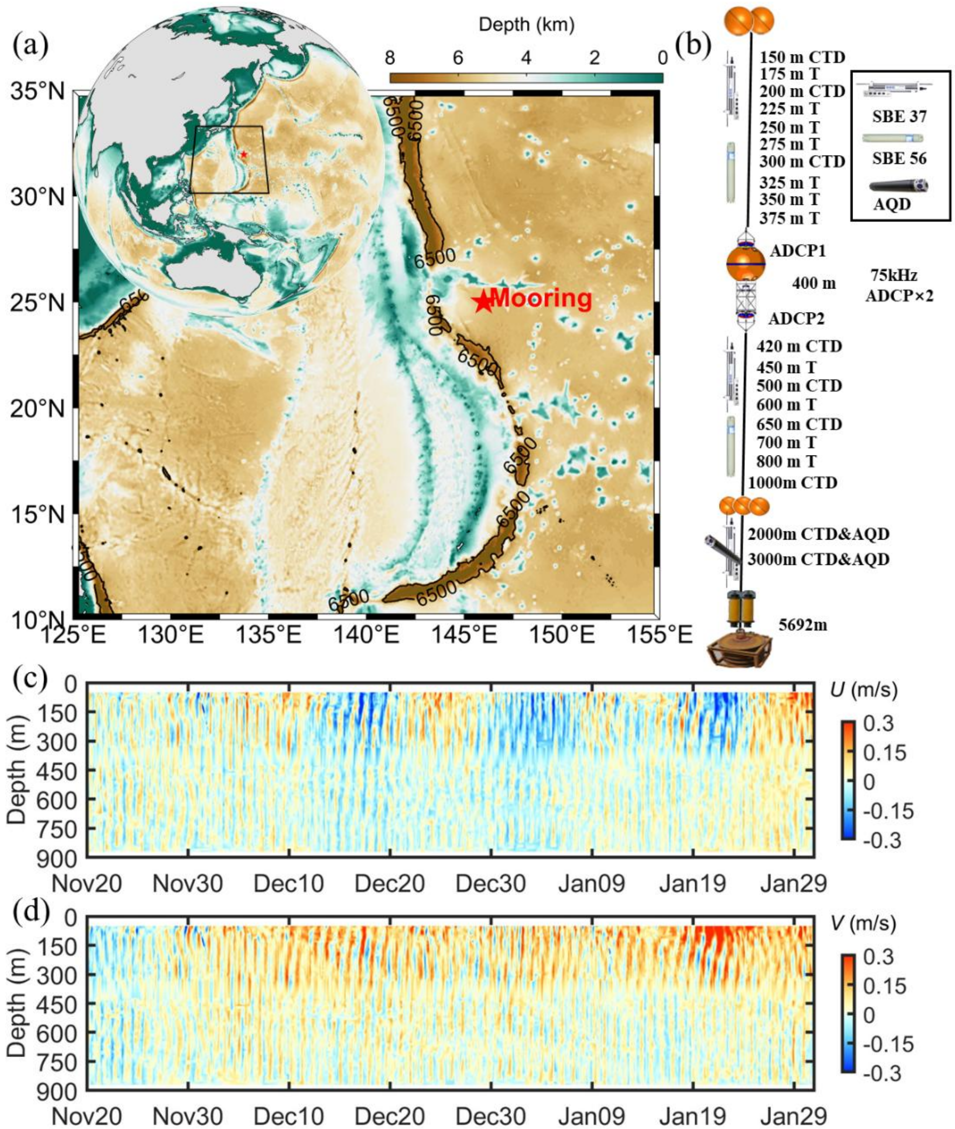

Figure 1. (a) Location of subsurface mooring (marked by a red pentagram), with color shading representing the topography. (b) Deployment depths of instruments on the subsurface mooring. (c) and (d) Depth-time plot of zonal and meridional velocities from 20 November 2017 to 31 January 2018.

Additionally, reanalysis data produced by the Met Office Coupled Atmosphere-Land-Ocean-Ice data assimilation (CPLDA) system were used to calculate the energy transfer rate between NIWs and mesoscale eddies. The product provides daily-averaged variables with a horizontal resolution of 0.25° × 0.25°, including mixed layer depth, three-dimensional temperature, salinity, and currents. In the present study, the mixed layer depth (MLD) is defined as the depth where temperature is 0.5 °C lower than the sea surface temperature (Watanabe and Hibiya, 2002). This criterion was applied consistently throughout the present analysis. To verify the validity of using the reanalysis data, we compared them with the observational data. The results show that the reanalysis data agree well with the observations in variables of potential density and geostrophic currents (see Fig. S1 in the supplemental material). Therefore, it is plausible to use reanalysis data to compute the energy transfer rate between NIWs and mesoscale eddies. Additionally, the World Ocean Atlas 2023 (WOA23) gridded climatological temperature and salinity fields were used to examine the modal decomposition of the near-inertial velocity field.

2.2 Modal decomposition

Vertical structure of internal waves can be represented by the superposition of multiple discrete baroclinic modes that only depend on the climatologic full-depth profile of stratification (D'Asaro et al., 1995; Figs. 2a and 2b). The vertical structure of each mode is constrained by (Gill, 1982; Thorpe & Jiang, 1998; Luo et al., 2024),

$$\frac{\partial^2 \Phi_{\mathrm{n}}(z)}{\partial z^2} + \frac{N^2(z)}{c_{\mathrm{n}}^2} \Phi_{\mathrm{n}}(z) = 0. \tag{1}$$

The boundary conditions at sea surface and sea bottom are $\Phi_{\mathrm{n}}(0) = 0$ and $\Phi_{\mathrm{n}}(-H) = 0$. Here, H is the water depth, n is the mode number, c_{n} is the eigenvalue, and N^2 is the buoyancy frequency square. $\mathit{\Phi}_{\mathrm{n}}$ represents the baroclinic mode of vertical displacement. The corresponding baroclinic modes for the horizontal velocity are

$$\mathit{\Pi}_{\mathrm{n}} = \rho_0 c_{\mathrm{n}}^2 \frac{d\mathit{\Phi}_{\mathrm{n}}(z)}{dz}, \tag{2}$$

where ρ_0 is the density. The vertical profiles of the first five baroclinic modes for Φ_{n} and $\mathit{\Pi}_{\mathrm{n}}$ are shown in Figs. 2(c) and 2(d). The horizontal near-inertial velocities can be expressed as

$$u(z,t) = \sum_{\mathrm{n}=0}^{N} u_{\mathrm{n}}(t) \mathit{\Pi}_{\mathrm{n}}(z). \tag{3}$$

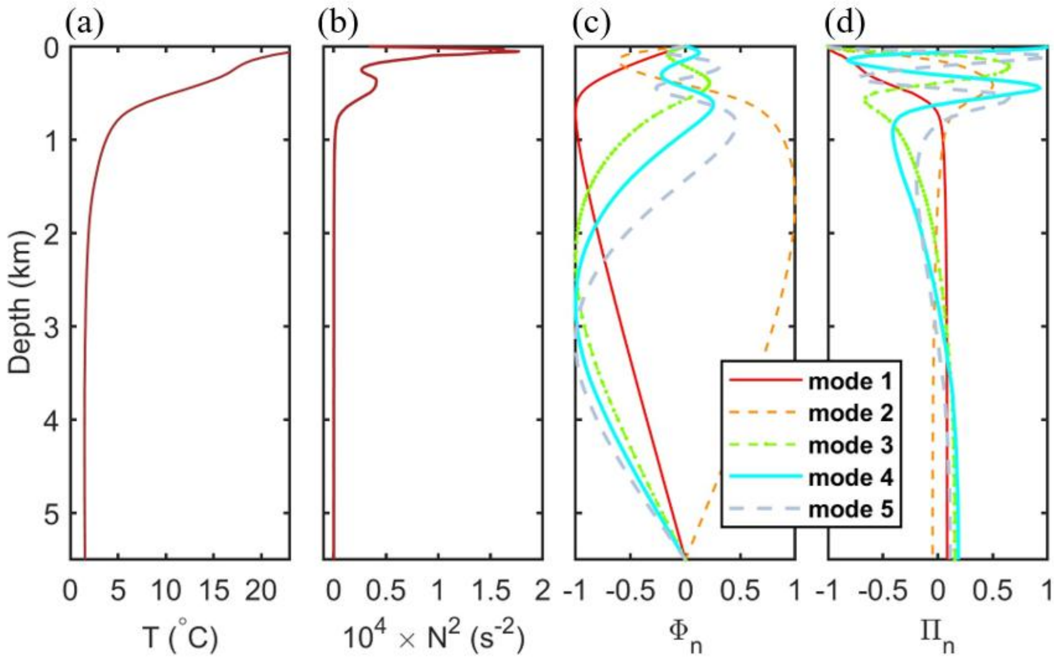

Figure 2. (a) Profile of potential temperature, T, from climatologic WOA23 data at the mooring site. (b) The same with (a), but for stratification N^2. (c) Normalized vertical structures of the first five baroclinic modes for vertical displacement. (d) The same as (c) but for horizontal velocity.

2.3 Energy transfer rate between mesoscale eddy and NIWs

Assuming that mesoscale eddies satisfy the geostrophic approximation, the corresponding energy transfer rate between mesoscale eddies and NIWs is given by Polzin (2010)

$$P = -(\langle u_{ni}u_{ni}\rangle - \langle v_{ni}v_{ni}\rangle)\frac{S_n}{2} - \langle u_{ni}v_{ni}\rangle S_s. \quad (4)$$

where $S_n = U_x - V_y$ and $S_s = U_y + V_x$ represent the normal and shear components of the horizontal strain, respectively. Here U and V are the horizontal velocity fields obtained from the reanalysis product. A 5-day temporal low-pass filter was applied to the reanalysis velocity fields to obtain the background horizontal velocity. The zonal and meridional near-inertial velocities, u_{ni} and v_{ni}, were extracted using a fourth Butterworth band-pass filter over the frequency range of [0.9 1.1] f_0. The angular bracket denotes a smoothing average over three inertial periods. Sensitivity experiments using low-pass windows of 3, 5, 7 days and averaging windows of 2–4 inertial periods confirm that the sign and principal temporal evolution of P are robust to these parameter choices (Fig. S3 in the supplemental material).

2.4 Near-inertial ellipse analysis

Assuming that the observed NIWs are linear plane waves, the intrinsic frequency ω_{i} of NIWs satisfies a simplified dispersion relation (Cuypers et al., 2013),

$$\omega_i^2 = f_{\mathrm{eff}}^2 + N^2 \frac{k_h^2}{(m^2 + k_h^2)}, \tag{5}$$

where f_{eff} is the effective Coriolis frequency, k_h is the horizontal wave number, m is the vertical wave number following Chen et al. (2023).

$$m = \partial(\mathrm{atan}(u_{\mathrm{ni}}/v_{\mathrm{ni}}))/\,\partial \mathrm{z}, \tag{6}$$

ω_{i} can be obtained by subtracting the Doppler shift from the observed frequency ω_{o},

$$\omega_{\mathrm{i}} = \omega_{\mathrm{o}} - |k_{\mathrm{h}}|\boldsymbol{V}\cos(\Phi - \theta), \tag{7}$$

where Φ is the horizontal propagation direction of wave packets, $\boldsymbol{V}$ and θ represent the velocity vector and direction of the mean current. By combining Eq. 5 and Eq.6, f_{eff} and k_h are given by (Alford and Gregg, 2001)

$$f_{\mathrm{eff}} = \frac{\omega_0}{\left(r + \frac{m|\boldsymbol{V}|}{N}\cos(\Phi - \theta)\sqrt{r^2 - 1}\right)}, \tag{8}$$

$$k_{\mathrm{h}}^2 = m^2(\omega_i^2 - f_{\mathrm{eff}}^2)/N^2, \tag{9}$$

where $r = \omega_{\mathrm{i}}/\,f_{\mathrm{eff}}$ is the major to minor axis ratio of an inertial ellipse. The vertical group velocities are given by Cuypers et al. (2013),

$$c_{gz} = -\frac{(N^2 - f_0^2)\beta^3}{k_h(1 + \beta^2)^{\frac{3}{2}}(f_0^2 + N^2\beta^2)^{\frac{1}{2}}}, \tag{10}$$

where $\beta = k_h/\,m$ is the angle of propagation to the vertical.

3 Results

3.1 Winter storms and wind-generated near-inertial energy into the mixed layer

According to the spatial and temporal distributions of wind fields, two wind storm events were identified during the observation period (Fig. 3). The first storm (hereafter called WS1) is from 6 December to 18 December, 2017, with the mean and maximum wind speeds of 8.5 m/s and 13.8 m/s, respectively, at the subsurface mooring site. Another storm (hereafter called WS2) occurs between 6 January and 17 January, 2018. The second storm is weak relative to the first storm, with the mean and maximum wind speeds of 6.9 m/s and 10.2 m/s, respectively. During the two storms, the wind speed and direction varied rapidly with time, thereby triggering corresponding near-inertial velocity responses in the mixed layer.

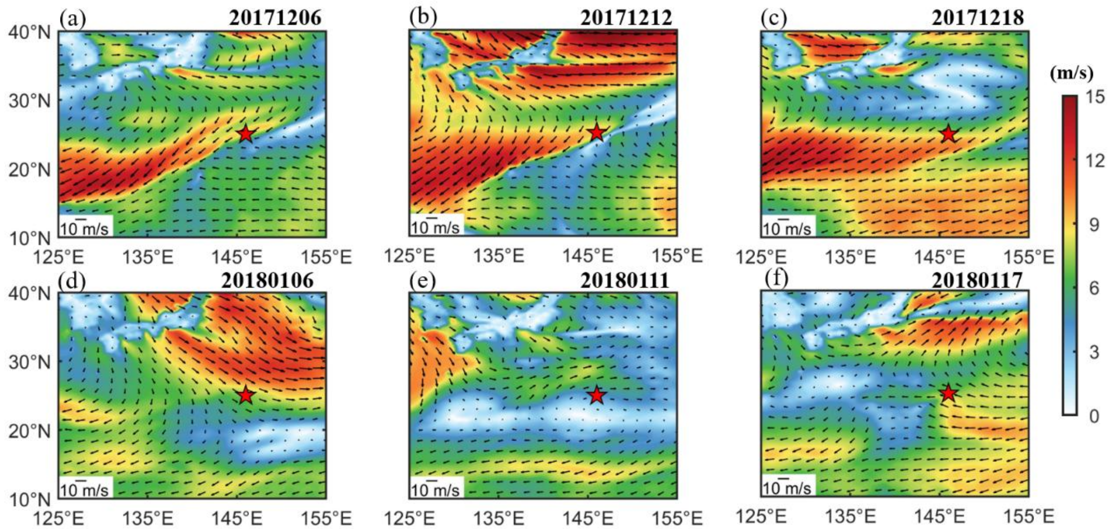

Figure 3. (a-c) Spatial and temporal distributions of wind speed from 6 December to 18 December, 2017, with arrows representing wind direction. (d-f) The same with (a-c), but corresponding to the distributions from 6 January to 17 January, 2018.

To illustrate the generation of NIWs at the subsurface mooring site, near-inertial velocity response and wind power input into the mixed layer calculated by a slab model are shown in Figs. 4(a-c). Alford et al. (2012) observed that the near-inertial velocities in the mixed layer estimated from the slab model show a high agreement with observations. During WS1 and WS2, the generated near-inertial velocities in the mixed layer reach up to ~0.6 m/s and ~0.2 m/s, respectively. The duration of strong near-inertial motions during WS1 is evidently longer than that during WS2. The mean wind power inputs into the mixed layer are 11.2×10^{-3} W/m^2 and 3.3×10^{-3} W/m^2 during WS1 and WS2, respectively. To compare the total wind-generated near-inertial energy input, the wind power is calculated cumulatively (Fig. 4d). The total near-inertial energy input into the mixed layer amounts to 11.5 kJ/m^2 during WS1 and 3.1 kJ/m^2 during WS2, respectively. Therefore, compared to the near-inertial energy input during WS2, the energy input during WS1 is approximately three times higher.

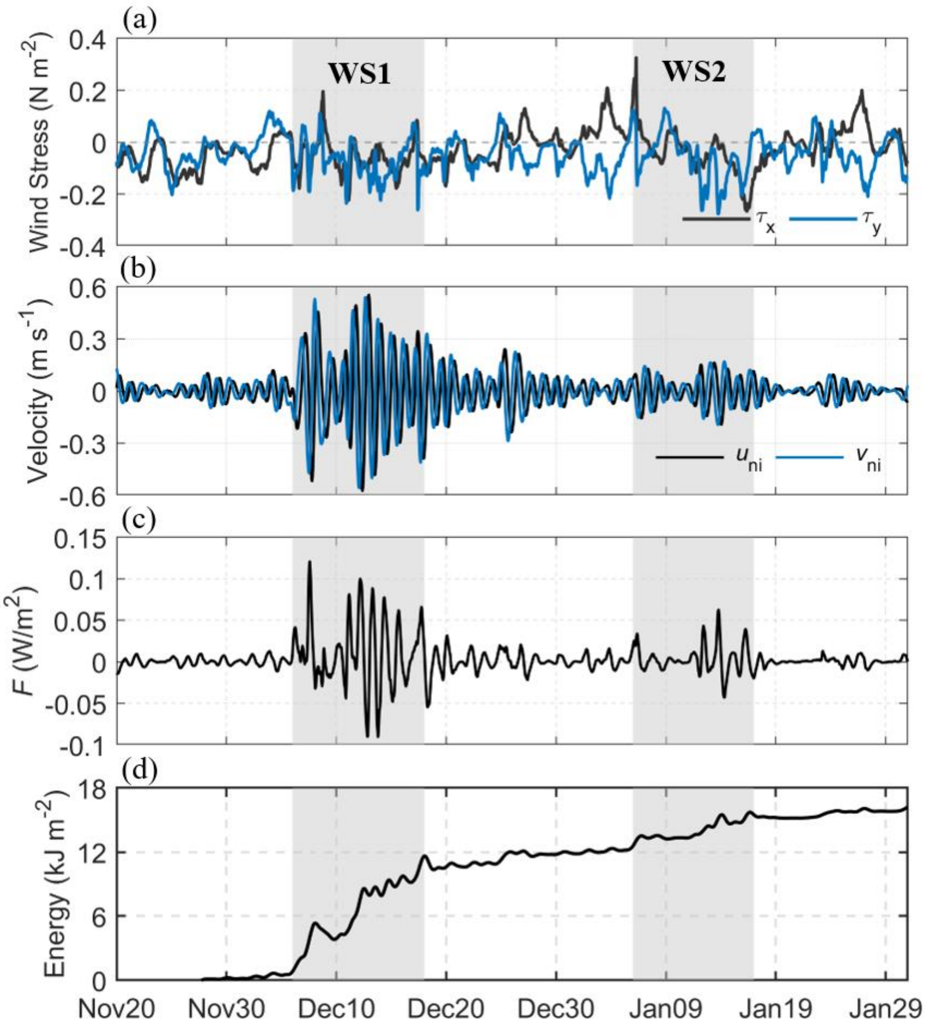

Figure 4. (a) Zonal (black line) and meridional (blue line) components of wind stress, (τ_x, τ_y), from 20 November, 2017 to 31 January, 2018. (b) Zonal and meridional near-inertial velocities, (u_{ni}, v_{ni}), calculated by a slab model. (c) Near-inertial energy flux, $F = \tau \cdot v_{ni}$. (d) Cumulative near-inertial energy input into the mixed layer.

3.2 Observations of two energetic NIW events in winter

Figures 5(a-c) show the observed near-inertial velocities and near-inertial kinetic energy ($\mathrm{NIKE} = 0.5\rho \times (u_{ni}^2 + v_{ni}^2)$, where ρ is a reference density). Corresponding to the passage of WS1 and WS2, two prominent near-inertial events are clearly resolved in observations. The first event occurs between 6 December and 25 December 2017. Before 10 December, the near-inertial energy is confined above 80 m depth, followed by a rapid downward propagation before 20 December. At a depth of 120 m, near-inertial velocity and NIKE reach their maximum values, at 0.4 m/s and 20 J/m^3, respectively. The second event developed from 6 to 24 January 2018, during which the maximum near-inertial velocity and NIKE reach up to 0.21 m/s and

21 J/m^3 at a depth of 220 m, respectively. According to MacKinnon et al. (2013), the total near-inertial velocities are further processed by rotary decompositions to obtain downward propagating and upward propagating NIKE (Figs. 5d and 5e). Consistent with the general features of NIWs in the upper ocean, the total NIKE is dominated by the downward propagating component. According to Johnston et al., 2021, the value of one-tenth of the maximum NIKE was used as the criterion for energy propagation depth. The propagation depths for the two NIW events are basically comparable, both located at a depth of approximately 300 m (Fig. 5d). Additionally, the decay time is defined as the time it takes for the near-inertial energy to decrease from its maximum value to one-tenth of the maximum value along the downward propagation path. Based on this definition, the decay times are approximately 9 days for WS1 and 5 days for WS2.

It should be noted that although the wind-generated near-inertial energy input into the mixed layer during WS1 is about three times larger than that during WS2, the observed NIKE intensity is comparable (Figs. 4d and 5c). This means that during the downward propagation processes, additional energy may be transferred into the second NIW event or transferred out from the first NIW event. It will be further investigated in detail in the discussion section.

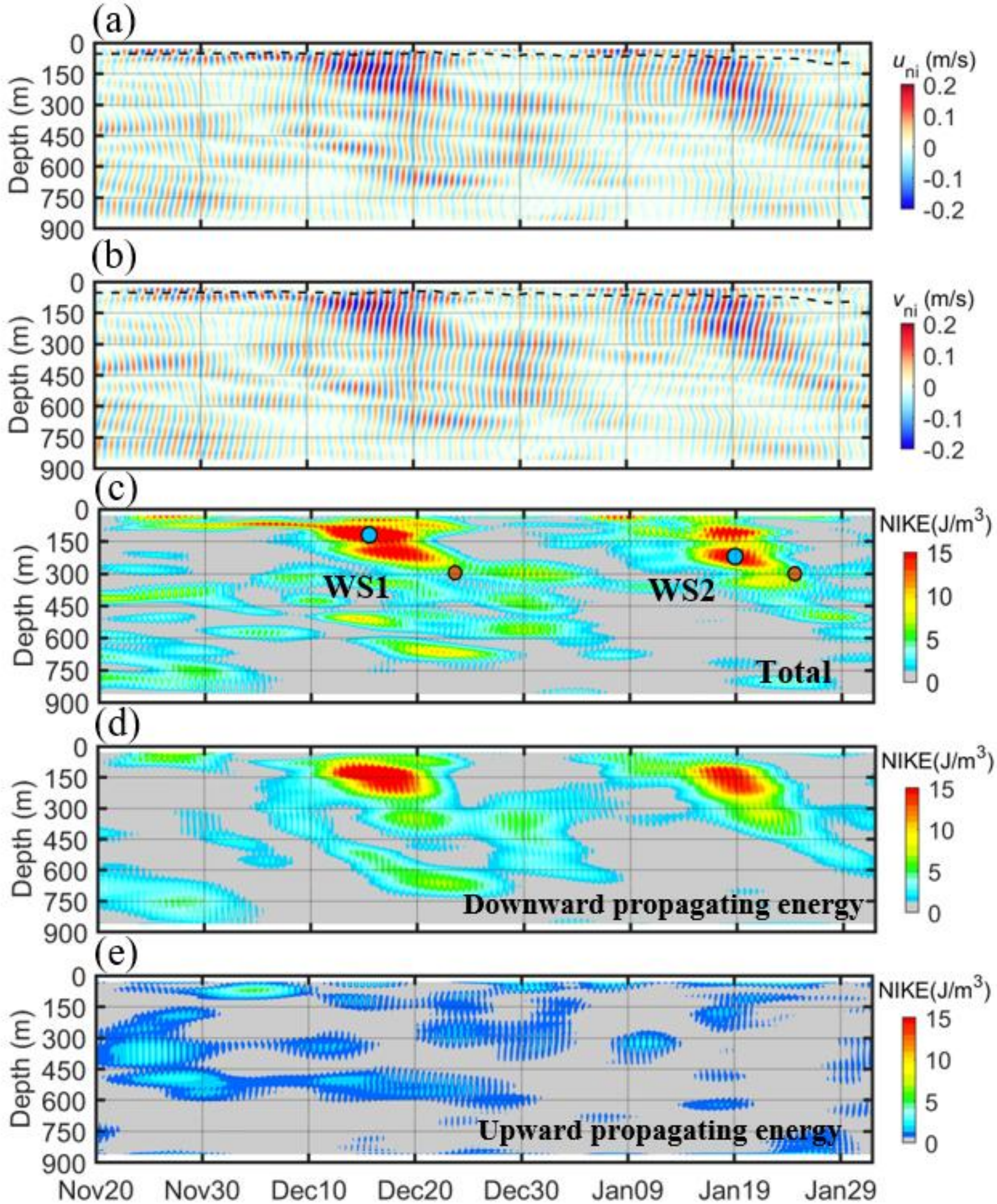

Figure 5. Depth-time plots of near-inertial velocities and near-inertial kinetic energy, NIKE, from 20 November 2017 to 30 January 2018. (a) Zonal near-inertial velocity, u_{ni}. (b) Meridional near-inertial velocity, v_{ni}. (c) Depth-time plot of NIKE. (d) and (e) are the same with (c), but for the downward-propagating and upward-propagating NIKE. The black dashed line in (a) and (b) indicates the mixed layer depth (MLD). The blue and brown circles in (c) indicate the time and depth of the maximum NIKE and one-tenth of the maximum NIKE for each NIW event, respectively.

3.3 Characteristics of the two NIWs

According to Gonella (1972), rotary frequency spectra of raw velocities from ADCPs during the two winter storms are shown in Fig. 6. Relative to the diurnal and semidiurnal tides, near-inertial energy exhibits significant clockwise polarization. The near-inertial energy in clockwise polarization is approximately one to two orders of magnitude larger than that in counterclockwise polarization, consistent with the general characteristics of NIWs in the Northern Hemisphere. During the two wind storms, the near-inertial energy notably exceeds tidal energy, especially in the upper 300 m, dominating the energy within the internal wave spectrum. Additionally, the near-inertial frequency shows a red shift during WS2, indicative of the existence of positive relative vorticity or positive Doppler shift according to the frequency relationship (Kunze, 1985).

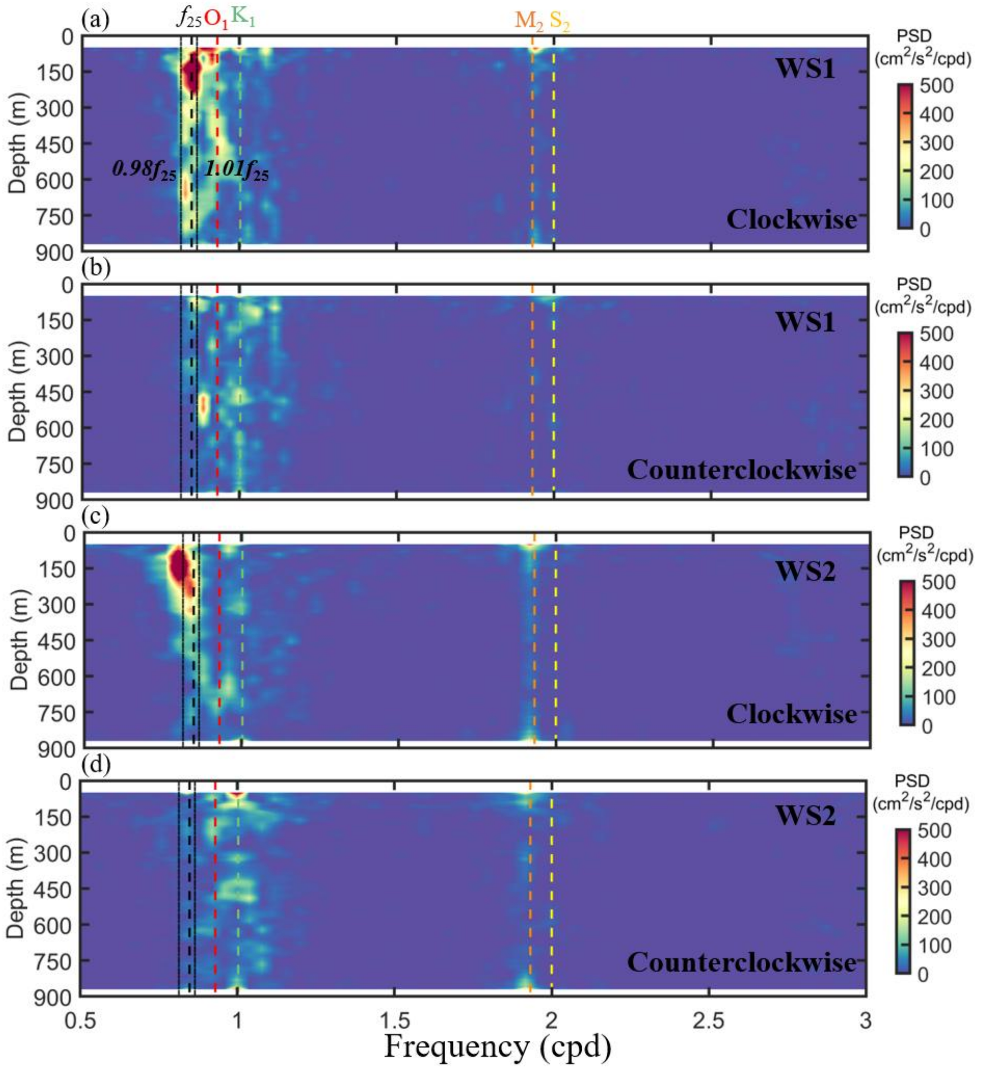

Figure 6. Rotary frequency spectra of raw velocities observed from ADCPs during WS1 (a and b) and WS2 (c and d). Clockwise and anticlockwise polarizations of velocities are shown in (a-d). The vertical dashed lines in panels represent the local inertial frequency, f_0, 0.98 f_0, 1.01 f_0, diurnal tidal frequency, O_1 and K_1, and semidiurnal tidal frequency, M_2 and S_2, respectively.

To further quantify the NIW properties during the two winter storms, the wavelengths, intrinsic frequency, and group velocities of the two near-inertial events are estimated by applying a near-inertial ellipse analysis (Fig. 7). Vertical wavelengths, λ_z, of NIWs can be estimated based on the vertical profiles of horizontal near-inertial velocities observed by ADCPs. For the two wave packets, their vertical wavelengths are 487 m and 372 m, respectively. According to directions of ellipse major axis combined with directions of background horizontal velocity (Chen et al., 2024), the propagation direction of near-inertial packets can be determined. Through least squares fitting following Hebert and Moum (1994), the observed frequency is extracted from the two NIW packets, with values of 1.01 f_0 and 0.98 f_0, respectively. Then, substituting the above parameters into Eqs. (7)-(9) yields the effective Coriolis frequency, intrinsic frequency, and horizontal wavelength, λ_H. Based on Eq. (10), vertical group velocity can be determined. For the two wave packets, the mean vertical group velocity are 31.2 m/day and 14.4 m/day, respectively, indicative of a slower vertical group velocity during WS2. Properties of the two wave packets are summarized in Table 1.

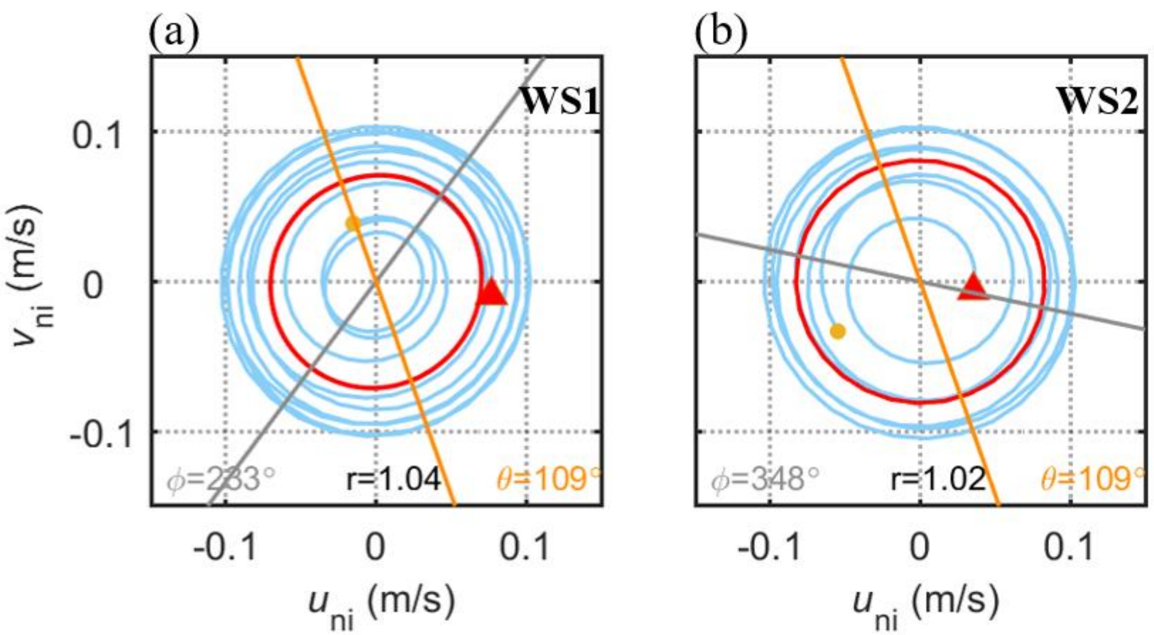

Figure 7. Depth-averaged near-inertial ellipses at the depth range of 70 m to 300 m during WS1 and WS2. The brown dot and red triangle indicate the beginning and end of ellipse, respectively. The red ellipse is obtained from the least squares fitting following Hebert and Moum (1994). The gray and orange lines represent the mean directions of the NIW propagation, *ϕ*, and the background horizontal current, *θ*, respectively. The ratio of major axis to minor axis of the near-inertial ellipse, *r*, is indicated in the corresponding panel.

Table 1. Properties of the two NIW events. Errors (±) represent one standard deviation estimated from the corresponding internal wave parameters during each NIW event.

Parameters	WS1	WS2
ϕ	233°	348°
ω_0/f_0	1.01	0.98
r	1.04	1.02
θ	109°±6°	109°±2°
λ_H	244±142 km	211±96 km
λ_z	487±70 m	372±62 m
ω_i/f_0	1.04±0.02	1.01±0.01
f_{eff}/f_0	1.01±0.01	0.98±0.01
C_{gz}	31.2±0.3 m/day	14.4±0.1 m/day

Next, the horizontal near-inertial velocities during WS1 and WS2 are projected onto the first 20 vertical baroclinic modes to investigate the modal characteristics of NIWs. Figures 8(a) and 8(b) show the depth-averaged NIKE for the first 10 vertical baroclinic modes during WS1 and WS2, respectively. For the two NIW events, the NIKE in the first 10 modes accounted for 75% and 80% of the total NIKE, suggesting that the first 10 modes reconstructed the NIWs well. During WS1, the near-inertial energy is dominated by low modes, with the first four modes contributing 48% of the total energy, while modes five to eight together account for only 24%. In contrast to the modal content during WS1, the near-inertial energy during WS2 exhibits a characteristic dominated by high modal energy, with the fifth to eighth modes contributing 41% of the total energy. Considering the difference in vertical wavelengths of the two NIW events, it is reasonable that the first NIW event with a larger vertical wavelength manifests a dominance of low modes. Correspondingly, the downward group velocity of the first wave packet is faster than that of the second wave packet.

Additionally, many previous researches suggest that the proportion of low modes in the total energy is correlated with MLD (Guthrie and Morison, 2021; Chen et al., 2025). In general, a shallow MLD shapes a short vertical wavelength of internal waves. However, as shown in Fig. 8(c), the mean MLD during WS2 is approximately 70 m, which is deeper than that during WS1, with a depth of about 51 m. This is contrasted with the conventional expectation that deep mixed layer tends to favor a higher low-mode contribution. The discrepancy suggests that except for the MLD, other factors may be more important to control the modal content of the two NIW events. Further examination is discussed in Section 4.

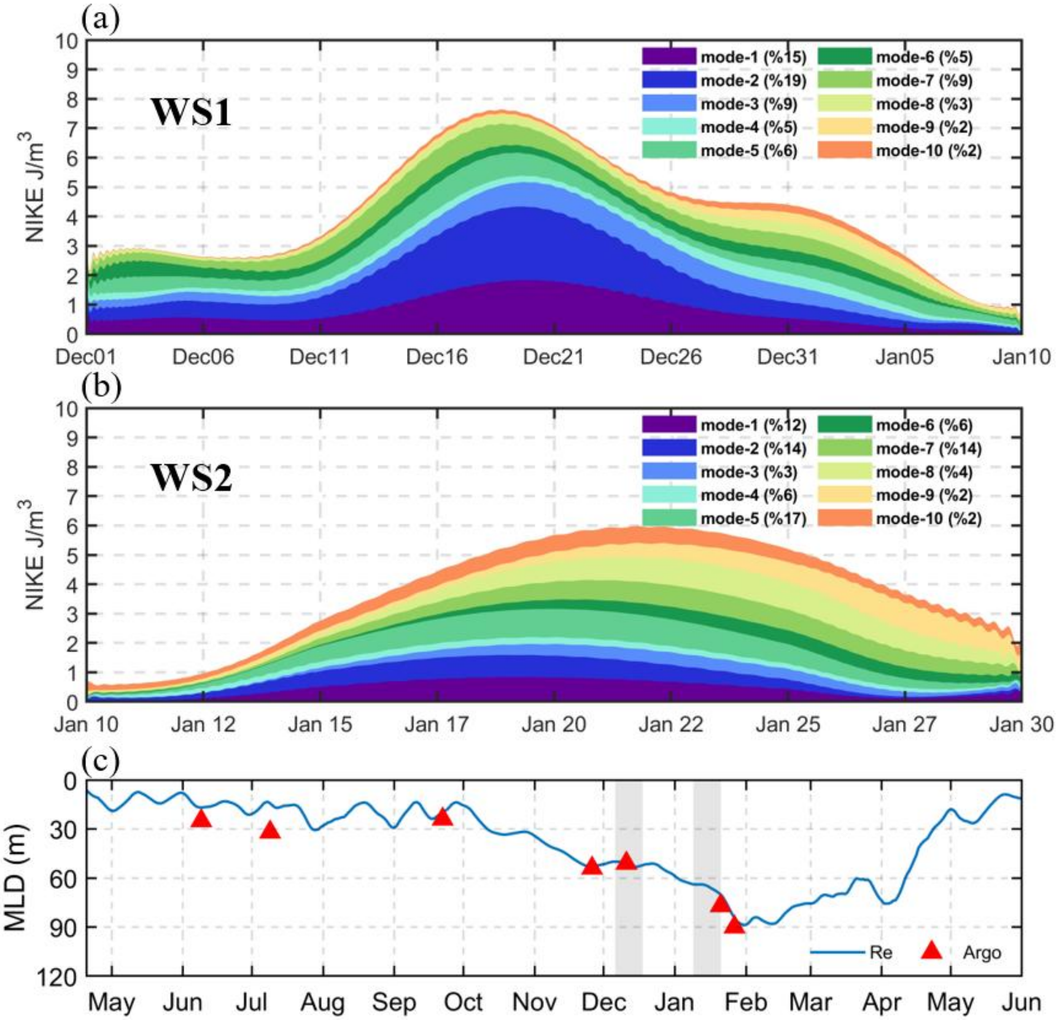

Figure 8. Depth-averaged near-inertial kinetic energy, NIKE, for the first 10 modes during WS1 (a) and WS2 (b). (c) Mixed layer depth during the full observational period calculated from reanalysis data (blue line), and Argo profiles (red triangles). Gray shading represents two storm events. Proportion of each mode's NIKE in the total NIKE is labeled in (a) and (b).

4 Discussion

4.1 Energy exchange between mesoscale eddies and NIWs

To understand the comparable NIKE intensity observed in the thermocline despite discernible difference in cumulative wind-generated energy input into the mixed layer during the two winter storms, energy transfer rate between mesoscale eddies and NIWs is examined. Through energy exchange between low-frequency flows and internal waves, energy can be transferred both from low-frequency flows to internal waves and from internal wave to low-frequency flows, with the highest efficiency occurring between mesoscale eddies and NIWs (e.g., Polzin, 2010).

Temporal variations of depth-averaged energy transfer rate between mesoscale eddies and NIWs within the mixed layer, P, are shown in Fig. 9(a), with negative values indicating an energy transfer from near-inertial motions to the mesoscale eddies, and vice versa. P is permanently negative during WS1 and is basically positive during WS2. It suggests that the mesoscale eddy energy is transferred to near-inertial motions during WS2, while the opposite occurs during WS1. Additionally, the intensity of P during WS1 is considerably higher than that during WS2. Consistent with the findings of Jing et al. (2018), the strong P primarily occurs in period of positive OW parameter when strain dominates relative vorticity (Fig. 9b). Furthermore, vertical variations of the time-averaged P during WS1 and WS2 are shown in Figs. 9(c) and 9(d), respectively, exhibiting significant energy transfer in the upper ~200 m depth. The depth-averaged values of P during WS1 and WS2 are -2.3×10^{-8} m^2s^{-3} and 0.24×10^{-8} m^2s^{-3}, respectively.

Many studies suggest that approximately 25% of wind-generated near-inertial energy in the mixed layer can radiate to the thermocline layer (e.g., Alford et al., 2012; Jing et al., 2018). Under this assumption, the two storms can generate near-inertial energy of approximately 2.8×10^{-3} W/m^2 and 0.82×10^{-3} W/m^2 into the thermocline layer during WS1 and WS2, respectively (Fig. 4). Considering that the enhanced NIKE associated with both NIW events is mainly distributed within the upper ~300 m (Fig. 5c), the P is vertically integrated over the upper 300 m. After vertically integrating of P in the upper 300 m, $\int_{300}^{0} \rho P dz$, the energy exchange between mesoscale eddies and NIWs is -1.3×10^{-3} W/m^2 during WS1 and 0.36×10^{-3} W/m^2 during WS2, respectively. Thus, approximately 46% of the wind-generated near-inertial energy is converted into mesoscale eddy during WS1. However, mesoscale eddies contribute approximately 43% of the wind-generated near-inertial energy to NIWs during WS2. Combining the wind energy input and mesoscale eddy's energy transfer, the total near-inertial energy input is approximately 1.5×10^{-3} W/m^2 during WS1 and 1.2×10^{-3} W/m^2 during WS2.

Furthermore, the time-integrated energy was calculated to compare the cumulative energy contribution over the two NIW events. The time-integrated wind-generated near-inertial energy flux, $\int F dt$, is -2.9 and 0.8 kJ/m^2 for WS1 and WS2, respectively. The time-integrated energy transfer, $\iint \rho P dz dt$, is 1.3 and 0.5 kJ/m^2, respectively. This indicates that mesoscale eddies remove a substantial fraction of wind-generated near-inertial energy in WS1, whereas they provide an additional energy source for NIWs in WS2. These estimates indicate that the eddy-wave interactions reduce the difference between NIKE in WS1 and WS2 and may therefore contribute to the comparable observed NIKE.

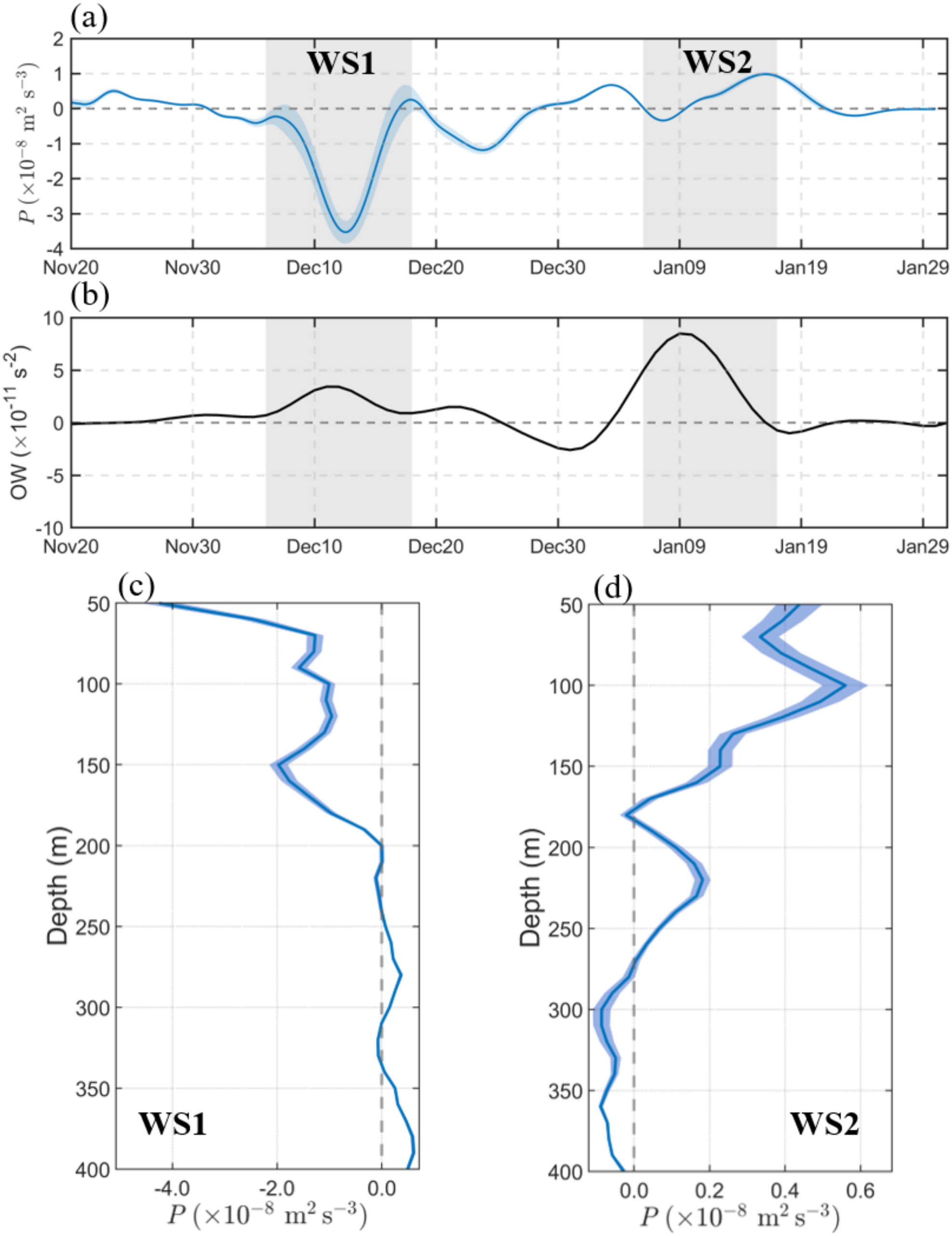

Figure 9. Energy exchange rate, P, between mesoscale eddies and NIWs. (a) Temporal variation of depth-averaged P within the mixed layer from 20 November 2017 to 31 January 2018. (b) Temporal variation of the Okubo-Weiss parameter, defined as OW = $S_n^2 + S_s^2 - \zeta^2$, where $S_n = U_x - V_y$, $S_s = V_x + U_y$ and $\zeta = V_x - U_y$. (c) Vertical profile of time-averaged P during WS1. (d) Vertical profile of time-averaged P during WS2. Blue shading in (a), (c), and (d) represents one standard deviation of the mean value.

4.2 Energy loss through turbulent dissipation and untrapped waves

The analysis above focuses on the energy exchange between mesoscale eddies and NIWs. However, near-inertial energy may also be influenced by other pathways, including turbulent dissipation and the radiation of untrapped waves away from the observation site (Kunze et al., 1995). Because direct turbulence measurements were not available, we could not directly quantify turbulent dissipation from microstructure observations. Instead, we estimated the parameterized dissipation rate using the Gregg–Henyey–Polzin (GHP) parameterization based on the observed velocity and stratification fields (Henyey et al., 1986; Gregg, 1989; Polzin et al., 2014; Kunze et al., 1995). It should be noted that the GHP estimate reflects the dissipation associated with the internal wave shear and therefore includes contributions from NIWs, diurnal tides, and semidiurnal tides.

The dissipation rates during WS1 and WS2 are 3.9×10^{-10} and 5.0×10^{-10} m^2/s^3, respectively (Fig. 10a). The corresponding time-integrated energy dissipation values are 4.1×10^{-4} and 4.3×10^{-4} m^2/s^2, respectively. These comparable values indicate that the energy loss associated with turbulent dissipation is of a similar magnitude during these two NIW events. Therefore, the pathway of turbulent dissipation is unlikely to be the primary reason for the comparable magnitude of NIKE during WS1 and WS2.

To further identify the dominant shear component of internal waves, the total vertical shear was decomposed into the near-inertial, diurnal and semidiurnal components. The corresponding vertical shear variances were calculated as $S_{\mathrm{ni}}^2 = |\partial u_{\mathrm{ni}}/\partial z|^2 + |\partial v_{\mathrm{ni}}/\partial z|^2$, $S_{\mathrm{D}}^2 = |\partial u_{\mathrm{D}}/\partial z|^2 + |\partial v_{\mathrm{D}}/\partial z|^2$, and $S_{\mathrm{M}}^2 = |\partial u_{\mathrm{M}}/\partial z|^2 + |\partial v_{\mathrm{M}}/\partial z|^2$, where S_{ni}^2, S_{D}^2, and S_{M}^2 represent the near-inertial, diurnal, and semidiurnal shear variances, respectively. The mean near-inertial shear variances during WS1 and WS2 are approximately three to four times larger than those of diurnal and semidiurnal components (Fig. 10b). This dominance of near-inertial shear suggests that near-inertial motions in enhancing the total shear and the associated dissipation rate during the two storm events.

In addition to turbulent dissipation, the radiation of untrapped waves may also contribute to the loss of locally observed near-inertial energy. The modal analysis shows that WS1 is characterized by a higher contribution from low modes, whereas WS2 contains a larger proportion of high-mode energy (Figs. 8a and 8b). Low-mode NIWs are generally more efficient at propagating away from their generation region, while high-mode NIWs are more likely to generate strong local shear and dissipate locally. Thus, near-inertial energy during WS1 may exhibit stronger outward propagation compared to that during WS2. However, the outward radiation of near-inertial energy cannot be quantitatively evaluated from a single subsurface mooring.

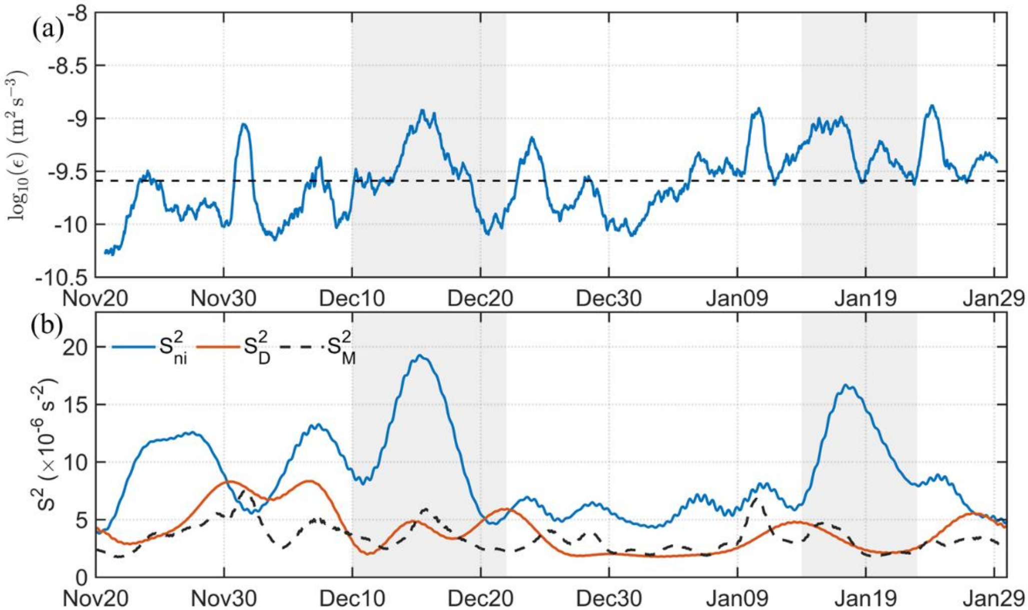

Figure 10. (a) Time series of the turbulent dissipation rate from GHP parameterization, during the observational period (50-300 m). The gray shading indicates the two NIW events. The horizontal dashed line denotes the time-averaged value. (b) Time series of vertical shear variance of near-inertial, diurnal, and semidiurnal components.

4.3. Roles of eddies and wind work modes in the NIW modal content

By analyzing the characteristics of NIWs, the modal content of NIWs during WS1 and WS2 is associated with the vertical wavelengths of NIWs. A large vertical wavelength corresponds to the dominance of low modes in NIWs. During the downward propagation of NIWs, the vertical wavelength is modulated by the relative vorticity of mesoscale eddies (D'Asaro, 1995; Kunze, 1985). The vertical variation of relative vorticity below the sea surface cannot be estimated directly from our observations. However, it is acknowledged that the relative vorticity increases with increasing depth in an anticyclonic eddy (ACE) and decreases with depth in a cyclonic eddy (CE). Thus, when NIWs are generated in an ACE, the increasing relative vorticity with depth can reduce the vertical wavelength of NIWs, resulting in the elimination of vertical group velocity and the formation of critical depth of NIWs (Kunze, 1985). Moreover, when NIWs propagate into an ACE from a region with positive relative vorticity, the relative vorticity gradually decreases along the propagation trajectory of NIWs, resulting in the increase of vertical wavelength (Chen et al., 2023). As shown in Figs. 11(a-e), the relative vorticity gradually decreases from positive to negative due to a westward-moving ACE passing over the subsurface mooring site during WS1. The depth-time distribution of relative vorticity derived from the reanalysis product is consistent with the surface vorticity, with positive to negative vorticity during WS1 and predominantly negative vorticity during WS2 (Fig. 11f). Therefore, in this situation the vertical wavelength of NIWs can gradually increase, subsequently leading to the dominance of low modes in NIWs.

However, the relative vorticity is negative during WS2, consequently reducing the vertical wavelength and favoring the dominance of high modes in NIWs (Zheng et al., 2023b).

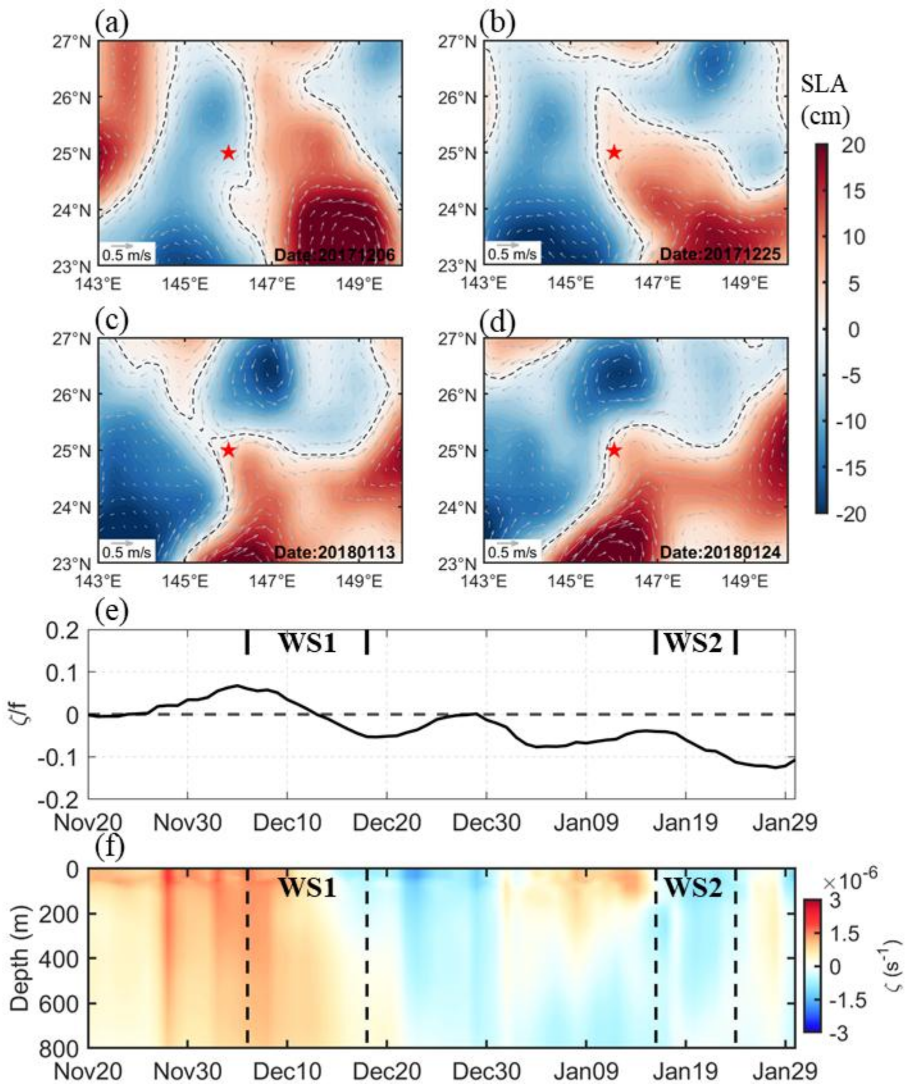

Figure 11. (a–d) Temporal-spatial distributions of sea level anomaly, SLA, with arrows indicating geostrophic currents. The red star represents the position of the subsurface mooring. (e) Temporal variation of relative vorticity calculated from surface geostrophic currents. (f) Depth-time distribution of relative vorticity derived from the reanalysis product.

Additionally, differences in modal projection of wind-generated near-inertial energy flux may also contribute to the difference in NIW modal content during WS1 and WS2. Following the modal decomposition method of Raja et al. (2022), the wind-generated near-inertial energy flux is projected onto the first 20 vertical baroclinic modes, $F_n(t) = \tau\,(t) \cdot v_{ni,n}$, where τ is the wind stress vector and $v_{ni,n}$ is the nth-mode near-inertial velocity at 50 m depth. Figure 12 shows the temporal variation of wind-generated near-inertial energy flux in the first ten modes. During WS1, the first four modes account for 50% of the total wind-generated near-inertial energy input, while modes five to eight together account for only 14%. However, during WS2 the fifth to eighth modes contribute 41% of the total wind-generated near-inertial energy input, indicating that wind forces exert a larger projection onto higher modes. Therefore, the discrepancies of modal content in the two NIW events could be interpreted as the joint result of the modal projection of wind-generated near-inertial energy and modulation by mesoscale eddies.

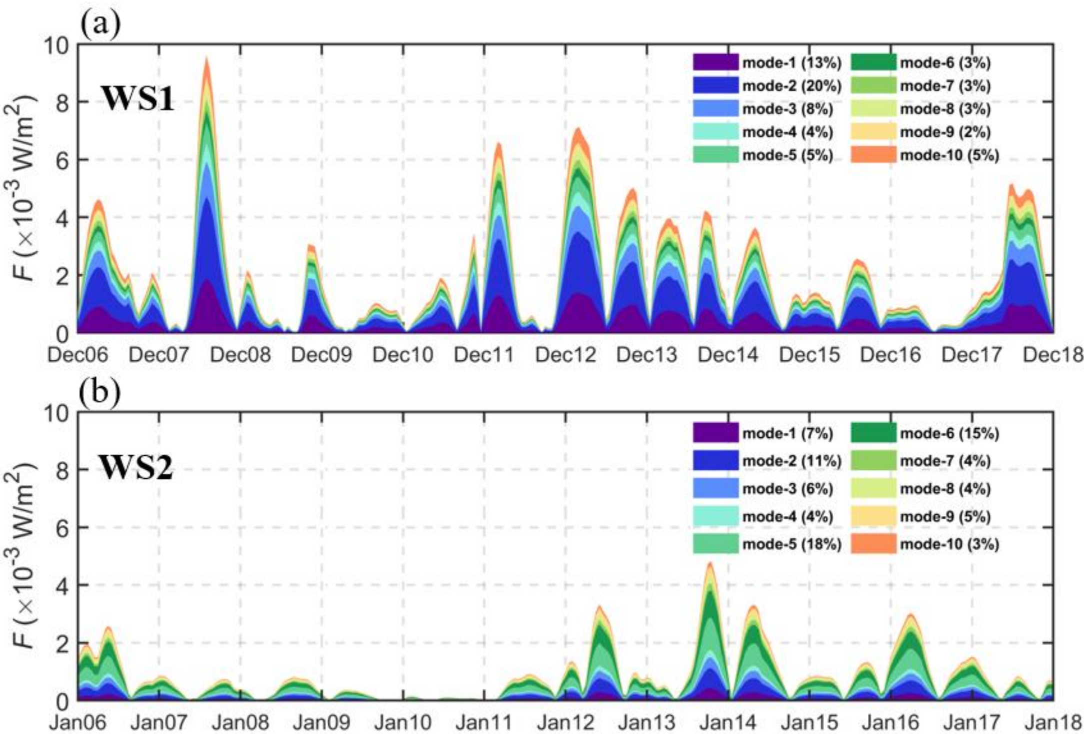

Figure 12. Temporal variation of wind-generated near-inertial energy flux, *F*, projected onto the first 10 modes during WS1 (a) and WS2 (b).

5 Summary

In this study, the generation and downward propagation characteristics of two NIW events during winter storms are examined using subsurface mooring observations combined with reanalysis data. Wind-generated near-inertial energy input suggests that the energy input into the mixed layer during WS1 is approximately three times higher than that during WS2, but the observed NIKE is comparable between the two events. The energy exchange between mesoscale eddies and NIWs indicates that approximately 46% of the wind-generated near-inertial energy is converted into mesoscale eddy during WS1, whereas mesoscale eddies contribute approximately 43% of the wind-generated near-inertial energy to NIWs during WS2.

The eddy-wave energy transfers may contribute to the comparable observed NIKE during the two events. However, turbulent dissipation and the radiation of energy out of the observed volume may also contribute to the comparable observed NIKE and cannot be fully quantified using the single mooring observations.

For the two NIW events, both the decay time, vertical wavelength, vertical group velocity of the first wave packet are larger than those of the second wave packet. Correspondingly, the first wave packet is dominated by low modes, while the second wave packet exhibits a characteristic of high mode dominance. The first four modes contribute 48% of the total near-inertial energy in the first NIW event. However, 41% of near-inertial energy is projected onto the fifth to eighth modes during WS2. It is found that modulation of eddies and modal content of wind-generated near-inertial energy input are of importance in determining the characteristics of modal content during the two NIW events. These findings highlight the combined roles of wind forcing and mesoscale eddy modulation in shaping energetic NIWs and have important implications for understanding wintertime interior mixing driven by breaking NIWs. Nevertheless, the analysis was based on observations from a single mooring site, which may not fully capture the spatial variability of NIW dynamics and their interaction with mesoscale structures across the broader region. Therefore, more observations and numerical studies on the dynamic characteristics of NIWs are needed in the future.

Data Availability Statement

The sea level and geostrophic velocity data are available at https://resources.marine.copernicus.eu/?option=com_csw&view=details&product_id=SEALEVEL_GLO_PHY_L4_NRT_OBSERVATIONS_008_046. The mixed layer depth data are obtained from the CMEMS, which can be downloaded from the CMEMS GLOBAL_ANALYSISFORECAST_PHY_CPL_001_015 product. ERA5 reanalysis data: https://cds. climate.copernicus.eu/cdsapp#!/dataset/reanalysis-era5-singlelevels?tab=overview; CPLDA reanalysis product: https://resources.marine.copernicus.eu/?option=com_csw&view=details&product_id=GLOBAL_ANALYSISFORECAST_PHY_CPL_001_015.

Author contributions

Hongkai Wang: Conceptualization, formal analysis, methodology, software, visualization, and writing – original draft, writing – review & editing. **Zifei Chen:** Conceptualization, formal analysis, writing – review & editing, and funding acquisition. **Xinyuan Diao:** Data curation and formal analysis. **Fei Yu:** Conceptualization, data curation, formal analysis, and writing – review & editing. **Xingchuan Liu:** Conceptualization, formal analysis, and writing – review & editing. **Qiang Ren:** Data curation, formal analysis, validation, and investigation. **Feng Nan:** Data curation and formal analysis.

Competing interests

The contact author has declared that none of the authors has any competing interests.

Disclaimer

Copernicus Publications remains neutral with regard to jurisdictional claims made in the text, published maps, institutional affiliations, or any other geographical representation in this paper. While Copernicus Publications makes every effort to include appropriate place names, the final responsibility lies with the authors. Views expressed in the text are those of the authors and do not necessarily reflect the views of the publisher.

Financial support

This work was jointly supported by the National Natural Science Foundation of China (Grant No. 42306008), China Postdoctoral Science Foundation (Grant Nos. 2023M743523, 2023M733525), and Natural Science Foundation of Shandong Province (ZR2023QD077).

References

Alford, M. H.: Redistribution of energy available for ocean mixing by long-range propagation of internal waves, Nature, 423, 156-159, 10.1038/nature01591, 2003a.

Alford, M. H.: Improved global maps and 54-year history of wind-work on ocean inertial motions, Geophysical Research Letters, 30, 10.1029/2002gl016614, 2003b.

Alford, M. H.: Sustained, Full-Water-Column Observations of Internal Waves and Mixing near Mendocino Escarpment, Journal of Physical Oceanography, 40, 2643-2660, 10.1175/2010jpo4502.1, 2010.

Alford, M. H.: Global Calculations of Local and Remote Near-Inertial-Wave Dissipation, Journal of Physical Oceanography, 50, 3157-3164, 10.1175/jpo-d-20-0106.1, 2020.

Alford, M. H. and Gregg, M. C.: Near-inertial mixing: Modulation of shear, strain and microstructure at low latitude, Journal of Geophysical Research: Oceans, 106, 16947-16968, 10.1029/2000jc000370, 2001.

Alford, M. H., Cronin, M. F., and Klymak, J. M.: Annual Cycle and Depth Penetration of Wind-Generated Near-Inertial Internal Waves at Ocean Station Papa in the Northeast Pacific, Journal of Physical Oceanography, 42, 889-909, 10.1175/jpo-d-11-092.1, 2012.

Alford, M. H., MacKinnon, J. A., Simmons, H. L., and Nash, J. D.: Near-Inertial Internal Gravity Waves in the Ocean, Annual Review of Marine Science, 8, 95-123, 10.1146/annurev-marine-010814-015746, 2016.

Barkan, R., Srinivasan, K., Yang, L., McWilliams, J. C., Gula, J., and Vic, C.: Oceanic Mesoscale Eddy Depletion Catalyzed by Internal Waves, Geophysical Research Letters, 48, 10.1029/2021gl094376, 2021.

Bieli, M., Sobel, A. H., Camargo, S. J., and Tippett, M. K.: A Statistical Model to Predict the Extratropical Transition of Tropical Cyclones, Weather and Forecasting, 35, 451-466, 10.1175/waf-d-19-0045.1, 2020.

Buijsman, M. C., Stephenson, G. R., Ansong, J. K., Arbic, B. K., Green, J. A. M., Richman, J. G., Shriver, J. F., Vic, C., Wallcraft, A. J., and Zhao, Z.: On the interplay between horizontal resolution and wave drag and their effect on tidal baroclinic mode waves in realistic global ocean simulations, Ocean Modelling, 152, 10.1016/j.ocemod.2020.101656, 2020.

Cao, A., Wang, S., Morimoto, A., Takikawa, T., and Guo, X.: Modal content of typhoon-induced near-inertial waves around the East China Sea, Continental Shelf Research, 264, 10.1016/j.csr.2023.105055, 2023.

Cao, A., Guo, Z., Pan, Y., Song, J., He, H., and Li, P.: Near-Inertial Waves Induced by Typhoon Megi (2010) in the South China Sea, Journal of Marine Science and Engineering, 9, 10.3390/jmse9040440, 2021.

Chen, S. and Qiu, B.: Interannual Variability of the North Pacific Subtropical Countercurrent and Its Associated Mesoscale Eddy Field, Journal of Physical Oceanography, 40, 213-225, 10.1175/2009jpo4285.1, 2010.

Chen, Z., Chen, Z., Yu, F., Qiang, R., Liu, X., Nan, F., Wang, J., Si, G., and Hu, Y.: Deep propagation of wind-generated near-inertial waves in the Northern South China Sea, Deep Sea Research Part I: Oceanographic Research Papers, 204, 10.1016/j.dsr.2023.104226, 2024.

Chen, Z., Yu, F., Chen, Z., Wang, J., Nan, F., Ren, Q., Hu, Y., Cao, A., and Zheng, T.: Downward Propagation and Trapping of Near-Inertial Waves by a Westward-Moving Anticyclonic Eddy in the Subtropical Northwestern Pacific Ocean, Journal of Physical Oceanography, 53, 2105-2120, 10.1175/jpo-d-22-0226.1, 2023.

Chen, Z., Chen, Z., Yu, F., Liu, X., Wang, J., Ren, Q., Liu, Y., Wang, R., Nan, F., Diao, X., and Ouyang, Z.: Observed Inhibited Downward Penetration of Wind-Generated Near-Inertial Energy in the Bering Sea, Geophysical Research Letters, 52, 10.1029/2025gl114896, 2025.

Cheung, H. M., Ho, C.-H., and Chu, J.-E.: Extratropical transition pathways of tropical cyclones and their associated storm intensity and destructiveness, iScience, 28, 10.1016/j.isci.2025.112814, 2025.

Cuypers, Y., Le Vaillant, X., Bouruet-Aubertot, P., Vialard, J., and McPhaden, M. J.: Tropical storm-induced near-inertial internal waves during the Cirene experiment: Energy fluxes and impact on vertical mixing, Journal of Geophysical Research: Oceans, 118, 358-380, 10.1029/2012jc007881, 2013.

D'Asaro, E. A.: The Energy Flux from the Wind to Near-Inertial Motions in the Surface Mixed Layer, Journal of Physical Oceanography, 15, 1043-1059, 10.1175/1520-0485(1985)015<1043:Tefftw>2.0.Co;2, 1985.

D'Asaro, E. A., Eriksen, C. C., Levine, M. D., paulson, C. A., Niiler, P., and Van Meurs, P.: Upper-Ocean Inertial Currents Forced by a Strong Storm. Part I: Data and Comparisons with Linear Theory, Journal of Physical Oceanography, 25, 2909-2936, 10.1175/1520-0485(1995)025<2909:Uoicfb>2.0.Co;2, 1995.

de Boyer Montégut, C., Madec, G., Fischer, A. S., Lazar, A., and Iudicone, D.: Mixed layer depth over the global ocean: An examination of profile data and a profile-based climatology, Journal of Geophysical Research: Oceans, 109, 10.1029/2004jc002378, 2004.

de Lavergne, C., Falahat, S., Madec, G., Roquet, F., Nycander, J., and Vic, C.: Toward global maps of internal tide energy sinks, Ocean Modelling, 137, 52-75, 10.1016/j.ocemod.2019.03.010, 2019.

Delpech, A., Barkan, R., Renault, L., McWilliams, J., Siyanbola, O. Q., Buijsman, M. C., and Arbic, B. K.: Wind-current feedback is an energy sink for oceanic internal waves, Scientific Reports, 13, 10.1038/s41598-023-32909-6, 2023.

Egbert, G. D. and Ray, R. D.: Estimates of M2 tidal energy dissipation from TOPEX/Poseidon altimeter data, Journal of Geophysical Research: Oceans, 106, 22475-22502, 10.1029/2000jc000699, 2001.

Ferrari, R. and Wunsch, C.: Ocean Circulation Kinetic Energy: Reservoirs, Sources, and Sinks, Annual Review of Fluid Mechanics, 41, 253-282, 10.1146/annurev.fluid.40.111406.102139, 2009.

Furuichi, N., Hibiya, T., and Niwa, Y.: Model-predicted distribution of wind-induced internal wave energy in the world's oceans, Journal of Geophysical Research: Oceans, 113, 10.1029/2008jc004768, 2008.

Garrett, C.: What is the “Near-Inertial” Band and Why Is It Different from the Rest of the Internal Wave Spectrum?, Journal of Physical Oceanography, 31, 962-971, 10.1175/1520-0485(2001)031<0962:Witnib>2.0.Co;2, 2001.

Gill, A. E.: Atmosphere-Ocean Dynamics, 10.1016/s0074-6142(08)x6002-4, 1982.

Gonella, J.: A rotary-component method for analysing meteorological and oceanographic vector time series, Deep Sea Research and Oceanographic Abstracts, 19, 833-846, 10.1016/0011-7471(72)90002-2, 1972.

Gregg, M. C.: Scaling turbulent dissipation in the thermocline, Journal of Geophysical Research: Oceans, 94, 9686-9698, 10.1029/JC094iC07p09686, 1989.

Guthrie, J. D. and Morison, J. H.: Not Just Sea Ice: Other Factors Important to Near-inertial Wave Generation in the Arctic Ocean, Geophysical Research Letters, 48, 10.1029/2020gl090508, 2021.

Hebert, D. and Moum, J. N.: Decay of a Near-Inertial Wave, Journal of Physical Oceanography, 24, 2334-2351, 10.1175/1520-0485(1994)024<2334:Doaniw>2.0.Co;2, 1994.

Henyey, F. S., Wright, J., and Flatté, S. M.: Energy and action flow through the internal wave field: An eikonal approach, Journal of Geophysical Research: Oceans, 91, 8487-8495, 10.1029/JC091iC07p08487, 1986.

Jiang, J., Lu, Y., and Perrie, W.: Estimating the energy flux from the wind to ocean inertial motions: The sensitivity to surface wind fields, Geophysical Research Letters, 32, 10.1029/2005gl023289, 2005.

Jing, Z., Chang, P., DiMarco, S. F., and Wu, L.: Observed Energy Exchange between Low-Frequency Flows and Internal Waves in the Gulf of Mexico, Journal of Physical Oceanography, 48, 995-1008, 10.1175/jpo-d-17-0263.1, 2018.

Johnston, T. M. S., Wang, S., Lee, C. Y., Moum, J. N., Rudnick, D. L., and Sobel, A.: Near-Inertial Wave Propagation in the Wake of Super Typhoon Mangkhut: Measurements From a Profiling Float Array, Journal of Geophysical Research: Oceans, 126, 10.1029/2020jc016749, 2021.

Kawaguchi, Y., Yabe, I., Senjyu, T., and Sakai, A.: Amplification of typhoon-generated near-inertial internal waves observed near the Tsushima oceanic front in the Sea of Japan, Sci Rep, 13, 8387, 10.1038/s41598-023-33813-9, 2023.

Kunze, E.: Near-Inertial Wave Propagation In Geostrophic Shear, Journal of Physical Oceanography, 15, 544-565, 10.1175/1520-0485(1985)015<0544:Niwpig>2.0.Co;2, 1985.

Kunze, E., Schmitt, R. W., and Toole, J. M.: The Energy Balance in a Warm-Core Ring's Near-Inertial Critical Layer, Journal of Physical Oceanography, 25, 942-957, 10.1175/1520-0485(1995)025<0942:Tebiaw>2.0.Co;2, 1995.

Liu, G., Chen, Z., Lu, H., Liu, Z., Zhang, Q., He, Q., He, Y., Xu, J., Gong, Y., and Cai, S.: Energy Transfer Between Mesoscale Eddies and Near-Inertial Waves From Surface Drifter Observations, Geophysical Research Letters, 50, 10.1029/2023gl104729, 2023.

Liu, Y., Jing, Z., and Wu, L.: Wind Power on Oceanic Near-Inertial Oscillations in the Global Ocean Estimated From Surface Drifters, Geophysical Research Letters, 46, 2647-2653, 10.1029/2018gl081712, 2019.

Luo, Z., Yang, D., Xu, L., Li, Y., Zhang, H., Wang, J., and Yin, B.: Baroclinic Rossby Waves With Phase Lag Cause Seasonal Upward-Propagating Signals in the Mid-Depth Equatorial Pacific Ocean, Journal of Geophysical Research: Oceans, 129, 10.1029/2023jc020418, 2024.

MacKinnon, J. A. and Gregg, M. C.: Shear and Baroclinic Energy Flux on the Summer New England Shelf, Journal of Physical Oceanography, 33, 1462-1475, 10.1175/1520-0485(2003)033<1462:Sabefo>2.0.Co;2, 2003.

MacKinnon, J. A., Alford, M. H., Pinkel, R., Klymak, J., and Zhao, Z.: The Latitudinal Dependence of Shear and Mixing in the Pacific Transiting the Critical Latitude for PSI, Journal of Physical Oceanography, 43, 3-16, 10.1175/jpo-d-11-0107.1, 2013.

Munk, W. and Wunsch, C.: Abyssal recipes II: energetics of tidal and wind mixing, Deep Sea Research Part I: Oceanographic Research Papers, 45, 1977-2010, 10.1016/s0967-0637(98)00070-3, 1998.

Musgrave, R., Pollmann, F., Kelly, S., and Nikurashin, M.: The lifecycle of topographically-generated internal waves, in: Ocean Mixing, 117-144, 10.1016/b978-0-12-821512-8.00013-x, 2022.

Oey, L. Y., Ezer, T., Wang, D. P., Fan, S. J., and Yin, X. Q.: Loop Current warming by Hurricane Wilma, Geophysical Research Letters, 33, 10.1029/2006gl025873, 2006.

Pollard, R. T. and Millard, R. C.: Comparison between observed and simulated wind-generated inertial oscillations, Deep Sea Research and Oceanographic Abstracts, 17, 813-821, 10.1016/0011-7471(70)90043-4, 1970.

Polzin, K. L.: Mesoscale Eddy–Internal Wave Coupling. Part II: Energetics and Results from PolyMode, Journal of Physical Oceanography, 40, 789-801, 10.1175/2009jpo4039.1, 2010.

Polzin, K. L., Naveira Garabato, A. C., Huussen, T. N., Sloyan, B. M., and Waterman, S.: Finescale parameterizations of turbulent dissipation, Journal of Geophysical Research: Oceans, 119, 1383-1419, 10.1002/2013jc008979, 2014.

Qiu, B.: Seasonal Eddy Field Modulation of the North Pacific Subtropical Countercurrent: TOPEX/Poseidon Observations and Theory, Journal of Physical Oceanography, 29, 2471-2486, 10.1175/1520-0485(1999)029<2471:Sefmot>2.0.Co;2, 1999.

Raja, K. J., Buijsman, M. C., Shriver, J. F., Arbic, B. K., and Siyanbola, O.: Near-Inertial Wave Energetics Modulated by Background Flows in a Global Model Simulation, Journal of Physical Oceanography, 52, 823-840, 10.1175/jpo-d-21-0130.1, 2022.

Rimac, A., von Storch, J. S., Eden, C., and Haak, H.: The influence of high-resolution wind stress field on the power input to near-inertial motions in the ocean, Geophysical Research Letters, 40, 4882-4886, 10.1002/grl.50929, 2013.

Shay, L. K. and Jaimes, B.: Near-Inertial Wave Wake of Hurricanes Katrina and Rita over Mesoscale Oceanic Eddies, Journal of Physical Oceanography, 40, 1320-1337, 10.1175/2010jpo4309.1, 2010.

Simmons, H. and Alford, M.: Simulating the Long-Range Swell of Internal Waves Generated by Ocean Storms, Oceanography, 25, 30-41, 10.5670/oceanog.2012.39, 2012.

Thomas, J. and Daniel, D.: Turbulent exchanges between near-inertial waves and balanced flows, Journal of Fluid Mechanics, 902, 10.1017/jfm.2020.510, 2020.

Thorpe, S. A. and Jiang, R.: Estimating internal waves and diapycnal mixing from conventional mooring data in a lake, Limnology and Oceanography, 43, 936-945, 10.4319/lo.1998.43.5.0936, 1998.

Vic, C., Naveira Garabato, A. C., Green, J. A. M., Waterhouse, A. F., Zhao, Z., Melet, A., de Lavergne, C., Buijsman, M. C., and Stephenson, G. R.: Deep-ocean mixing driven by small-scale internal tides, Nat Commun, 10, 2099, 10.1038/s41467-019-10149-5, 2019.

Watanabe, M. and Hibiya, T.: Global estimates of the wind-induced energy flux to inertial motions in the surface mixed layer, Geophysical Research Letters, 29, 10.1029/2001gl014422, 2002.

Whalen, C. B., de Lavergne, C., Naveira Garabato, A. C., Klymak, J. M., MacKinnon, J. A., and Sheen, K. L.: Internal wave-driven mixing: governing processes and consequences for climate, Nature Reviews Earth & Environment, 1, 606-621, 10.1038/s43017-020-0097-z, 2020.

Wunsch, C.: The Work Done by the Wind on the Oceanic General Circulation, Journal of Physical Oceanography, 28, 2332-2340, 10.1175/1520-0485(1998)028<2332:Twdbtw>2.0.Co;2, 1998.

Zheng, H., Zhu, X.-H., Zhao, R., Chen, J., Wang, M., Ren, Q., Liu, Y., Nan, F., Yu, F., and Park, J.-H.: Near-Inertial Waves Reaching the Deep Basin in the South China Sea after Typhoon Mangkhut (2018), Journal of Physical Oceanography, 53, 2435-2454, 10.1175/jpo-d-22-0136.1, 2023a.

Zheng, T., Yu, F., Ren, Q., Nan, F., Chen, Z., Liu, Y., Hu, Y., and Ding, Y.-n.: Near-inertial waves generated by typhoon MITAG under the influence of anticyclonic eddy east of Taiwan, Frontiers in Marine Science, 10, 10.3389/fmars.2023.1117197, 2023b.

Zheng, T., Yu, F., Ren, Q., Nan, F., Wang, J., Liu, Y., Chen, Z., and Tang, Y.: Observed near-inertial kinetic energy in the Philippine Sea, Regional Studies in Marine Science, 55, 10.1016/j.rsma.2022.102492, 2022.